ACS OMEGA

Open Access

http://pubs.acs.org/journal/acsodf

Article

One-Pot Hydrothermal Method Preparation of Cerium−Nitrogen-Codoped Carbon Quantum Dots from Waste Longan Nucleus as a Fluorescent Sensor for Sensing Drug Rifampicin

Xue-Hua Sun,* Min Ma, Rui Tian, Hong-Mei Chai, Jian-Wei Wang, and Lou-Jun Gao

Cite This: *ACS Omega* 2023, 8, 34859−34867

Read Online

ACCESS | Metrics & More | Article Recommendations | Supporting Information

ABSTRACT: Currently, the large-scale application of carbon quantum dots (CQDs) is usually limited by their low quantum yield and detection limit. Herein, the abandoned longan nucleus was used as a carbon source to synthesize cerium−nitrogen-codoped carbon quantum dots (Ce/N-CQDs) with strong luminescence intensity. In this work, the fluorescent properties and fluorescent quantum yield of CQDs may be improved by the single cerium-doped carbon quantum dots (Ce-CQDs) and the single nitrogen-doped carbon quantum dots (N-CQDs). Nevertheless, the Ce/N-CQDs exhibited intense fluorescence with a high quantum yield. Compared with CQDs, the quantum yield of Ce/N-CQDs was significantly increased from 5 to 32% and showed high photostability and good water solubility. The Ce/N-CQDs can be used for the direct detection of rifampicin (RFP) in human serum. The concentration demonstrated a good linear relationship in the range of 1.0×10^{-7}−9.0×10^{-6} mol/L, with a detection limit of 9.6×10^{-8} mol/L.

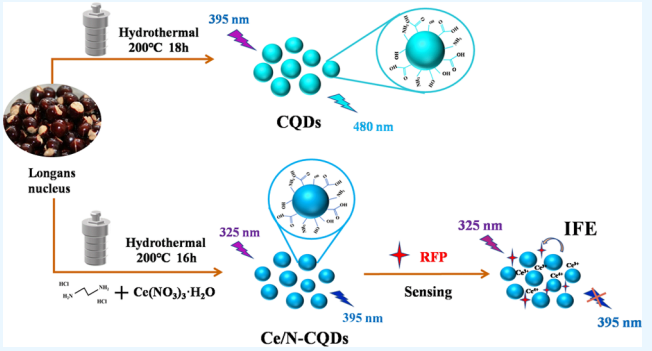

0. INTRODUCTION

Tuberculosis is a chronic infectious disease caused by *Mycobacterium tuberculosis*, which mainly infects the lungs.[1] Rifampicin (RFP) is one of the most effective drugs widely used against tuberculosis. It is a bactericidal antibiotic based on RNA polymerase that can enter cells[2] and can be combined with other antibiotics for the treatment of tuberculosis, staphylococcal endocarditis, osteomyelitis, and other diseases.[3] At present, the methods used to detect RFP include electrochemical method,[4] liquid chromatography,[5] chemiluminescence method,[6] etc. However, metallic- and nonmetallic-codoped carbon quantum dots (CQDs) used as fluorescence sensors for the direct detection of RFP have not been reported.

CQDs are smaller than 10 nm in size with photoluminescence properties of nanomaterials,[7] and CQDs have low cost, easy synthesis, adjustable fluorescence, good water solubility and biocompatibility and other excellent properties. Therefore, CQDs are widely used in biological sensing,[8,9] drug testing,[10] ion sensing,[11] biological imaging,[12] and pesticide detection,[13] etc. In the synthesis process of CQDs, a variety of biomass materials can be used, such as the capsids of viruses and algae,[14] since the biomass itself may contain heteroatoms such as N, P, and S, which makes biomass CQDs have self-doping characteristics.[15] Biomass CQDs also have certain limitations. Most biomass CQDs are synthesized by using water as a solvent that usually shows strong blue fluorescence. However, their quantum yield is low, which limits their application to some extent. Heteroatom doping and surface passivation of CQDs are usually used to improve the quantum yield and fluorescence properties of CQDs. For example, N,[16] B,[17] S,[18] P[19], and other nonmetal doping or metal[20] doping of CQDs can significantly improve the fluorescence quantum yield of CQDs and can also change the emission of CQDs to produce unique electronic properties. Nitrogen doping CQDs can greatly improve the fluorescence intensity and produce excitation independence properties due to passivated surface states. Various studies have demonstrated that the doping with metal ions can contribute to changing the band structure through chelation and coordination between metal ions and CQD surface groups as well as improve the fluorescence quantum yield. Metal ions have more empty orbitals and easily lose electrons. The carboxyl and amino groups on the surface of CQDs are also easy to chelate and coordinate with metal ions.[21] Therefore, metal doping is an excellent strategy for improving the fluorescence quantum yield and creating new optical property.[22] For example, Han[23] et al. prepared duplex metal-codoped CQDs, which confirmed that Ag(I) doping

Received: June 14, 2023
Accepted: August 25, 2023
Published: September 11, 2023

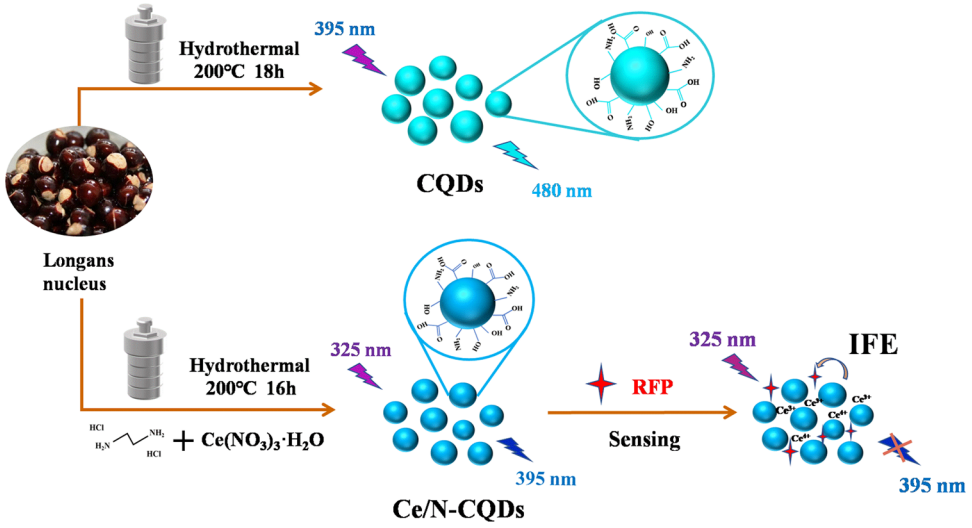

Figure 1. Mechanism of RFP detection by Ce/N-CQDs.

enhanced photoluminescence intensity by changing the gap between the conduction band and valence band. Wang[24] et al. doped the metal element Bi into CQDs, which makes them metallic and promotes charge transfer. Cerium has both trivalent and tetravalent states and is considered a good doping metal element in various materials. The outermost layer of trivalent cerium contains an unpaired 4f electron, which can easily coordinate with the carboxyl groups to change the electron distribution and surface structure.

Based on the above analysis results, cerium−nitrogen-codoped carbon quantum dots (Ce/N-CQDs) were prepared by hydrothermal method using longan nucleus powder as the carbon source, ethylenediamine as the nitrogen source, and cerium nitrate as the metal source. The binding modes, structures, morphologies, fluorescence lifetimes, and RFP quenching mechanisms of Ce/N-CQDs were investigated systematically. The codoping of Ce and N not only changed the structure of single CQDs, enriched their surface functional groups, and improved their fluorescence properties but also significantly improved the quantum yields of CQDs. Compared with CQDs, the quantum yield of Ce/N-CQDs was significantly increased from 5 to 32%. Ce/N-CQDs were highly sensitive and selective to drug RFP in serum; their preparation and response mechanisms are shown in Figure 1.

1. EXPERIMENTAL SECTION

1.1. Materials and Apparatus. *Materials.* Longans nucleus was selected from fresh longan in the local market. Ethylenediamine hydrochloride and cerium nitrate were acquired from Macklin (Shanghai, China). RFP was purchased from Beijing Tanmo Quality Inspection Co., Ltd. Tris was purchased from Shanghai Lanji Biotechnology Co., Ltd. All reagents used in the experiment, such as hydrochloric acid, glucose, starch, sucrose, β-cyclodextrin, lactose, sodium chloride, ferric chloride, magnesium sulfate, copper sulfate, calcium chloride, and aluminum chloride, were analytically pure, and the experimental water was ultrapure.

Apparatus. The fluorescence spectrum was obtained by a fluorescence spectrophotometer (PerkinElmer LS55, made in the U.K.). The absorption spectra of CQDs were tested using a UV−visible spectrophotometer (UV-2550, made in Japan). Fourier infrared spectrometry (IR Prestige-21, made in Japan), transmission electron microscope (JEOL JEM 2800, made in Japan), Raman spectrum (Horiba Lab RAM HR Evolution, made in Japan), X-ray powder diffractometer (XRD-7000, made in Japan), and X-ray photoelectron spectroscopy (Thermo Scientific ESCALAB Xi+, made in the USA) were used to characterize the structure of CQDs. The fluorescence lifetime of the sample was tested by using a steady-state transient fluorescence spectrometer (FLSP920, made in the U.K.). A thermostatic drying oven (DHG-9145AF, made in China) is used for preparing CQDs by the hydrothermal method.

1.2. Preparation of CQDs. CQDs were synthesized directly from longans nucleus using a one-step simple hydrothermal treatment. 1.2 g of longans nucleus and 25 mL of ultrapure water were added to a beaker, and then the mixture was sonicated to ensure equal dispersion. The solution was transferred to a Teflon-lined stainless autoclave, and the reaction was carried out at 200 °C for 18 h. The solution was centrifuged at 8000 rpm for 10 min after cooling to room temperature. A filter membrane (0.22 μm) was used to filter the supernatant, and the filtrate was kept for use at 4 °C. Finally, the clarified aqueous solution of CQDs with a yellowish-brown color was dried through a freeze-dryer to obtain a yellow solid sample.

1.3. Preparation of N-CQDs, Ce-CQDs, and Ce/N-CQDs. The Ce/N-CQDs were created by using a hydrothermal technique. Ultrasound was used to dissolve and distribute 1.2 g of longan nucleus, 0.4 g of ethylenediamine hydrochloride, and 0.3 g of cerium nitrate in 25 mL of ultrapure water. The solution was then transferred to a 50 mL Teflon-lined stainless steel autoclave, heated at 200 °C for 16 h, and centrifuged to obtain Ce/N-CQDs at room temperature. When not in use, the filtrate was stored at 4 °C. Vacuum drying was used to create solid samples for characterization. Ce-CQDs and N-CQDs were synthesized under these ideal conditions.

1.4. Quantum Yield Determination. The fluorescence quantum yields at excitation wavelengths of CQDs and Ce/N-CQDs were calculated using quinine sulfate as a reference compound. The absorption values and fluorescence peak integral areas of the CQDs and quinine sulfate were determined. According to the formula, the fluorescence

https://doi.org/10.1021/acsomega.3c04242
ACS Omega 2023, 8, 34859−34867

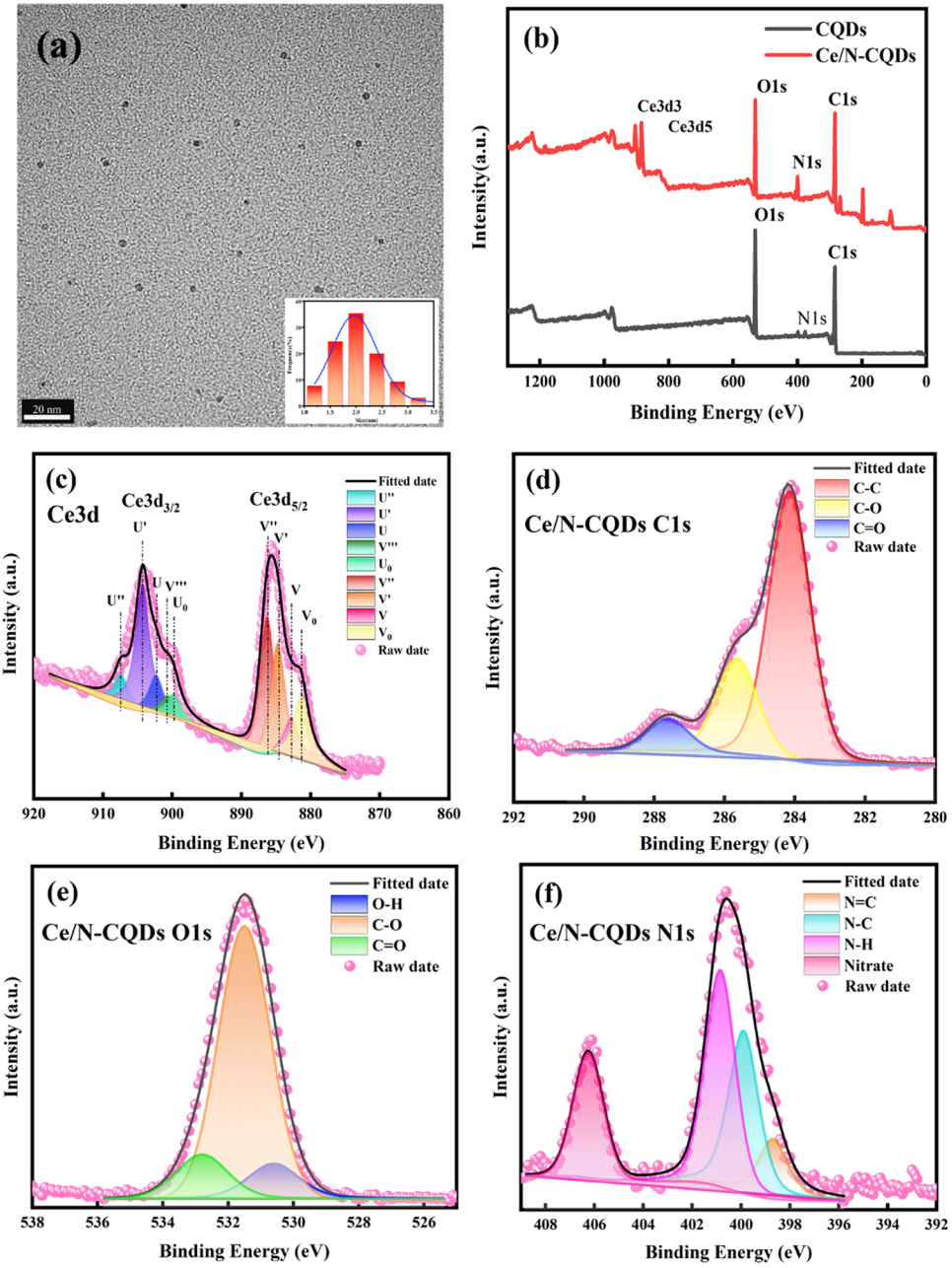

Figure 2. (a) TEM images of Ce/N-CQDs and particle size distribution histograms of Ce/N-CQDs. (b) Full XPS spectra of CQDs and Ce/N-CQDs. High-resolution spectrum of (c) Ce 3d and high-resolution XPS (d) C 1s, (e) O 1s, and (f) N 1s spectra of Ce/N-CQDs.

quantum yields of CQDs, Ce-CQDs, N-CQDs, and Ce/N-CQDs were calculated[25] (1). *Y* stands for the fluorescence quantum yield, *S* is the fluorescence peak integral area, and *A* in the formula stands for absorbance. 1 and 2 represent the substance to be measured and the reference substance, respectively

$$Y_1 = Y_2 \frac{S_1}{S_2} \frac{A_2}{A_1} \quad (1)$$

1.5. Study on the Fluorescence Sensing of RFP. To quantitatively detect RFP, 1.80 mL of Ce/N-CQDs solution (diluted 500 times), 1.00 mL of tris-HCl buffer solution (pH 7.4), and an appropriate amount of RFP standard solution were added to the 10.00 mL system. Then, it was diluted to the scale with ultrapure water, shaken well, and allowed to stand for 5 min before testing. At an excitation wavelength of 325 nm, the fluorescence was measured at emission wavelengths of 395 nm. The slits were fixed at 5 nm for both the excitation and emission. The fluorescence intensity ($\Delta F = F_0 - F$) had a good linear relationship with the RFP concentration, which was used to develop a sensor for determining the drug's RFP content.

1.6. Applications in Real Samples. Three kinds of RFP capsules were selected in the market, and the content of RFP in the capsules was analyzed by the developed method. In addition, this developed method was also used in serum actual sample determination. The blood samples were extracted from normal individuals and promptly centrifuged in a high-speed centrifuge at 8000 rpm for 15 min. The clarified yellow liquid in the upper layer was the serum. The serum was diluted 20-

https://doi.org/10.1021/acsomega.3c04242
ACS Omega 2023, 8, 34859−34867

fold with tris-HCl buffer and used for the spiked recovery assay of the actual sample RFP.[26]

2. RESULTS AND DISCUSSION

2.1. Synthesis of CQDs and Ce/N-CQDs. The codoped Ce/N-CQDs with strong fluorescence performance and high quantum yield were obtained in the conditions of optimizing the optimal dosage of longan nucleus, ethylenediamine hydrochloride, and cerium nitrate, as well as the optimal reaction temperature and time. The optimization of synthesis conditions is provided in the Supporting Information in more detail. These results showed that the fluorescence intensity of CQDs was the best when the dosage of longan nucleus was 1.2 g (Figure S1a); the reaction temperature and time were 200 °C (Figure S1d) and 18 h (Figure S1e), respectively. On the basis of the optimal amount of longan nucleus in CQDs, nitrogen and cerium were codoped. The results showed that when the reaction conditions were 200 °C for 16 h (Figure S1d,e), the optimal dosage of ethylenediamine hydrochloride as the nitrogen source was 0.4 g (Figure S1b), while the dosage of cerium nitrate as the metal source was 0.3 g (Figure S1c); the fluorescence intensity of Ce/N-CQDs prepared was the strongest. Under the influence of different factors, the fluorescence performance of CQDs doped with N and Ce was nearly four times higher than that of single CQDs, which could be attributed to the changes in morphology, composition, and structure of the doped CQDs. All of these factors can lead to different properties of CQDs. It can open a proper band gap in the electrical structure of CQDs. Ce doping minimizes the surface defects of CQDs, fills the well state, and increases the emissivity. Under the optimal synthesis conditions of Ce/N-CQDs, the fluorescence characteristics and subsequent detection of Ce/N-CQDs were carried out.

2.2. Characterization of CQDs and Ce/N-CQDs. The morphology and structure of Ce/N-CQDs were confirmed by transmission electron microscopy (TEM). The results are displayed in Figure 2a. The size distribution of the prepared Ce/N-CQDs was uniform, ranging from 1 to 3.5 nm, and the average size was reduced to 2.0 nm, which was 1.0 nm lower than the average size of the CQDs (Figure S2a) before doping. In addition, the crystal structures of CQDs and Ce/N-CQDs were further characterized by X-ray diffraction (XRD) (Figure S2b). The XRD pattern of CQDs showed broad peaks roughly centered at 28°, corresponding to the characteristic peaks of graphene (002) planes, which was consistent with reported results in the literature.[27] With the doping of Ce and N, the XRD peak position of CQDs shifted to the right and the intensity decreased, which indicated that the successful doping of CQDs led to the increase of the diffraction angle, the decrease of the crystal plane spacing, the decrease of grain size, and the decrease of crystallinity.

The structures of CQDs and Ce/N-CQDs were analyzed by Raman spectroscopy. As shown in Figure S2c, the ordered G-band of 1575 cm^{-1} of both CQDs and Ce/N-CQDs is stronger than the disordered D-band of 1386 cm^{-1}, but the G−D strength ratio of Ce/N-CQDs is 2.18, while that of the prepared CQDs is 2.07. The result showed that Ce/N-CQDs have higher graphitization degree and better crystallinity than CQDs. Since the D-band in the Raman spectrum is the common feature of sp^3 defects in carbon, the G-band provides plane vibration information on sp^2-bonded carbon. The higher the intensity ratio between G-band and D-band, the higher the degree of graphitization and the better the crystallinity in general.[28]

The surface functional groups and composition of these CQDs were investigated using FTIR spectra and an X-ray photoelectron spectroscopy pattern. As shown in Figure S2d, it was revealed by FTIR results that CQDs and Ce/N-CQDs exhibited a broad absorption band of intermolecular association O−H stretching vibrations at 3413 cm^{-1}. The absorption peak at 2052 cm^{-1} was attributed to the tensile vibration of the C═N bond. These absorption peaks between 1607 and 1595 cm^{-1} may be caused by the C═O stretching vibration of the amide in the associated state and the N−H bending vibration of the primary amine. The CQDs and Ce/N-CQDs exhibited σ(O−H) peaks, and σ(C−O) peaks were between 1095 and 1000 cm^{-1}. Compared with nondoped CQDs, Ce/N-CQDs showed an obvious C−H tensile vibration of unsaturated carbon and saturated carbon at 3010 and 2928 cm^{-1}, respectively. The absorption peaks between 1415 and 1335 cm^{-1} were attributed to the tensile vibration of the C−C and C−N bonds. From these, the surface of Ce/N-CQDs had rich oxygen- and nitrogen-containing functional groups, which improved the hydrophilicity and stability of the Ce/N-CQDs in an aqueous system. Ce/N-CQDs had a large number of sp^2-hybridized groups, including hydroxyl and carboxyl groups, which could be coordinated with cerium to change the surface of CQDs. Ce/N-CQDs perform better in terms of fluorescence thanks to the doping of N and Ce components. The chemical state and surface composition of CQDs and Ce/N-CQDs were compared and analyzed using XPS. From Figure 2b, it can be seen that compared with the XPS measurement spectra of CQDs, the XPS measurement spectra of Ce/N-CQDs contain not only C 1s (284 eV), N 1s (400 eV), and O 1s (531 eV), but also Ce 3d (885 and 904 eV), and the content of N 1s (400 eV) was significantly increased, which fully indicated the successful doping of cerium and nitrogen. According to the literature,[29] Ce (IV) has six characteristic peaks, while Ce (III) has four characteristic peaks. The electronic states of Ce $3d_{3/2}$ and Ce $3d_{5/2}$ are well separated, with an interval of 18.6 eV (Figure 2c). The peaks at V_0 (881.36 eV), V (882.77 eV), V′ (884.74 eV), and V″ (886.28 eV) are attributed to Ce $3d_{5/2}$. The characteristic peaks of Ce $3d_{3/2}$ are U_0 (899.78 eV), V‴ (900.63 eV), U (902.32 eV), U′ (904.29 eV), and U″ (907.38 eV). According to the literature,[30] the corresponding peaks at U″, U‴, V″, and V″ belonging to Ce (IV), U′, U_0, V′, and V_0, respectively, were the characteristic peaks of Ce (III), and U′ and V′ belong to the photoelectron emission of Ce (III). It was proven that cerium existed in the form of Ce^{3+} and Ce^{4+}. The proportions of Ce (III) and Ce (IV) in Ce/N-CQDs were 55.5% and 44.5%, respectively. The high-resolution spectra of C 1s, N 1s, and O 1s of CQDs and Ce/N-CQDs were fitted. The C 1s spectrum of Ce/N-CQDs (Figure 2d) gives the features of C−C at 284.15 eV, C−O at 285.60 eV, and C═O at 287.60 eV, which indicated the existence form of carbon atoms. There were three obvious peaks at 530.42 531.5, and 532.83 eV binding energies in the high-resolution spectra of O 1s (Figure 2e), which corresponded to the ═ 1s, C−O, and C═O. The N 1s spectrum as shown in Figure 2f was described by three typical peaks at 397.98 399.88, and 401.68 eV, representing the C═N, C−N, and N−H energy levels of C, respectively, and nitrate (406.64 eV) also increased slightly. Compared with CQDs, the content of C−O, O−H, and C═O in C 1s and O 1s spectra of Ce/N-CQDs decreased steadily (Figure S2e,f). It

https://doi.org/10.1021/acsomega.3c04242
ACS Omega 2023, 8, 34859−34867

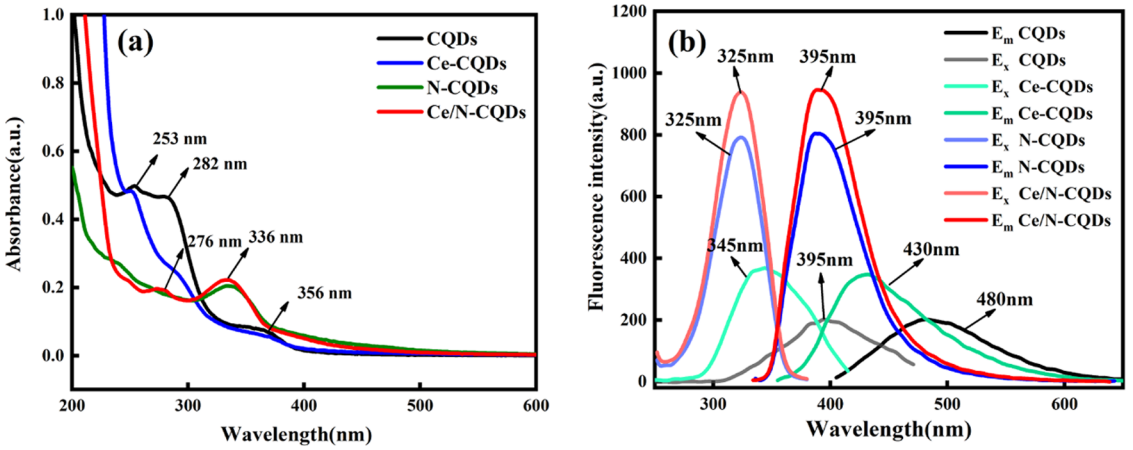

Figure 3. (a) UV−vis spectra of CQDs, Ce-CQDs, N-CQDs, and Ce/N-CQDs; (b) excitation and emission spectra of CQDs, Ce-CQDs, N-CQDs, and Ce/N-CQDs.

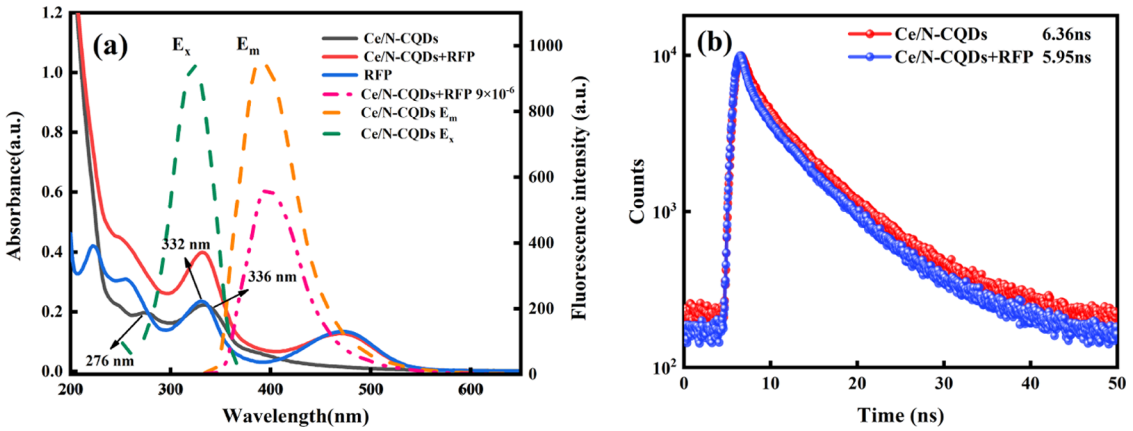

Figure 4. (a) UV−vis and fluorescence spectra of Ce/N-CQDs, Ce/N-CQDs + RFP, and RFP and (b) fluorescence decay curves of Ce/N-CQDs and Ce/N-CQDs + RFP.

has been demonstrated in the literature that the photoluminescence (PL) characteristics of CQDs may be either λ_{ex}-independent when the contents of C−O−C and C−O−H decline, which was consistent with the spectral characterization of Ce/N-CQDs.[31] As shown in Figure S2g, CQDs contain a small number of nitrogen atoms. With the addition of ethylenediamine and cerium nitrate (Figure 2f), the amount of each nitrogen functional group increased to varying degrees. Comprehensively considering the above analytical results, it was concluded that CQDs were successfully doped with Ce and N elements and Ce/N-CQDs consisted of a carbon core covered with rich hydrophilic functional groups.

2.3. Optical Properties of CQDs and Ce/N-CQDs. The optical properties of Ce- and N-codoped CQDs were investigated by UV−vis and fluorescence spectroscopy. The UV−vis absorption spectra of Ce/N-CQDs (Figure 3a) showed a strong absorption band at 336 nm, which was blue-shifted and enhanced compared to the absorption peak at 356 nm of CQDs, probably due to the derivatization of the carboxyl groups on the surface of CQDs into amide bonds by nitrogen doping. The peaks at 253 and 282 nm of CQDs were attributed to the $\pi-\pi^*$ leap of C═C, but the peak position was also blue-shifted and the absorption intensity was significantly weakened after the codoping of Ce and N. This might be due to the blue shift of the absorption peak because the doping of Ce with N caused the conjugation system in the precursor compound to become smaller, which caused the structural change or size reduction of CQDs.[32] The strong absorption band of Ce/N-CQDs at 336 nm was close to its optimal excitation wavelength of 325 nm, which is the fluorescence emission center of Ce/N-CQDs. From the fluorescence spectrogram (Figure 3b), it could be seen that the CQDs produced the maximum emission at 480 nm under the optimal excitation of 395 nm. When the excitation and emission peak positions of the CQDs doped with Ce and N, respectively, showed a blue shift and a significant enhancement of fluorescence intensity, the fluorescence intensity enhancement of the CQDs codoped with Ce and N was even greater with a blue shift of the maximum excitation wavelength to 325 nm and a blue shift of the emission wavelength to 395 nm. This might be caused by the quantum size effect of CQDs or it might be due to the electronegativity of N being greater than that of C and the doping of N caused a negative induction effect[33] and also promoted the radiative recombination luminescence of the electron−hole pairs on the surface of CQDs.

The fluorescence spectra of CQDs codoped with Ce and N (Figure S4) showed that the emission of PL was independent of excitation. As the excitation wavelength of Ce/N-CQDs increased, its fluorescence intensity reached a maximum at a 325 nm excitation wavelength and then gradually decreased, but its emission wavelength position at 395 nm did not shift.

https://doi.org/10.1021/acsomega.3c04242
ACS Omega 2023, 8, 34859−34867

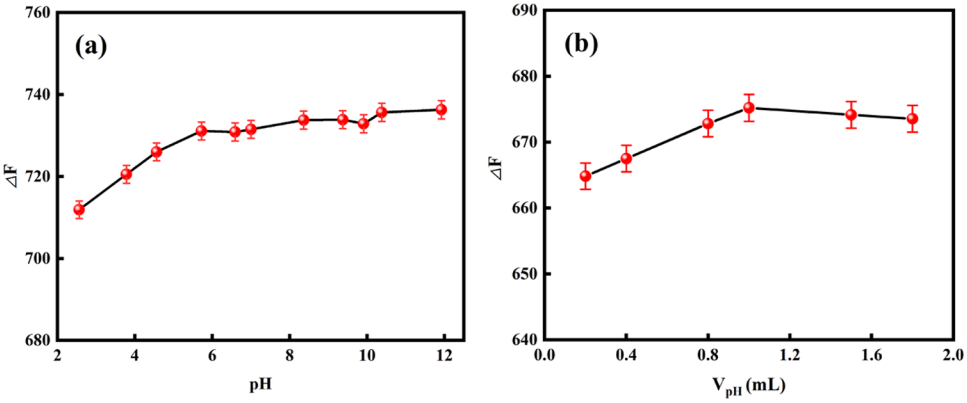

Figure 5. (a) Impacts of the pH value and (b) buffer solution dosage.

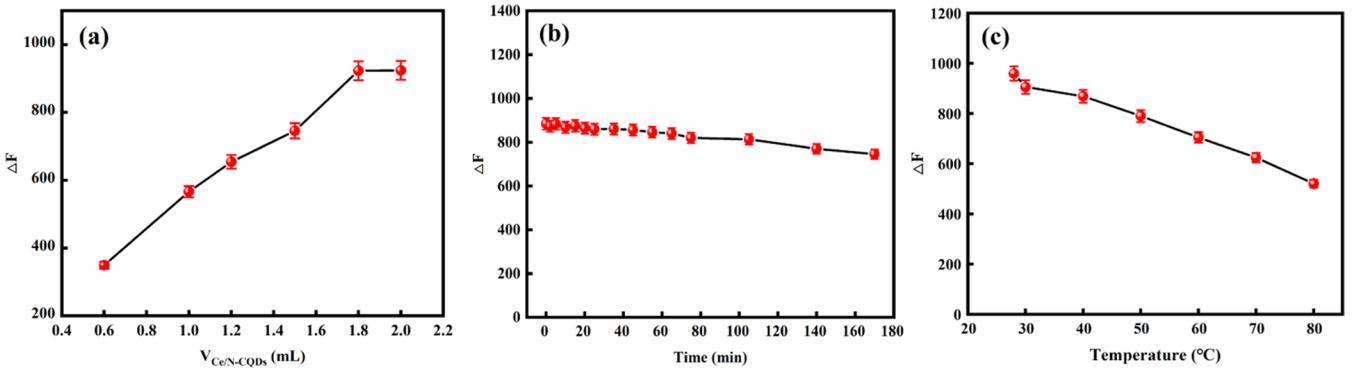

Figure 6. (a) Effects of the Ce/N-CQD dosage, (b) reaction time, and (c) reaction temperature on the detection performance of the sensor.

The fluorescence quantum yield of CQDs steadily increased from 5% to 32% with the doping of Ce and N. And the fluorescence quantum yield of Ce/N-CQDs was higher than that of Ce doping and N doping alone; the results are shown in Table S1.

2.4. Quenching Mechanism of Ce/N-CQDs + RFP. From the fluorescence spectra in Figure 4a, it can be seen that the drug RFP has a certain fluorescence quenching effect on Ce/N-CQDs, so the Ce/N-CQD fluorescent probes were constructed for the direct determination of drug RFP directly. Here, the fluorescence quenching mechanism of RFP on Ce/N-CQDs was investigated by UV−vis absorption spectra, fluorescence spectra, and fluorescence lifetime measurements. From the UV−vis absorption spectra (Figure 4a), it was seen that Ce/N-CQDs had absorption peaks at 336 and 276 nm, and RFP had characteristic absorption peaks at 256, 332, and 473 nm. When RFP was added to the Ce/N-CQD system, the absorption spectra of Ce/N-CQDs + RFP were the superposition of the UV absorption spectra of Ce/N-CQDs and RFP, and the addition of RFP did not change the original absorption spectra of Ce/N-CQDs, and the absorption spectra of the bursting agent RFP overlapped with the excitation spectra and emission spectra of Ce/N-CQDs. According to the analysis of the fluorescence decay curve in Figure 4b, the fluorescence lifetimes of Ce/N-CQDs before and after the addition of the burster RFP were 6.36 and 5.95 ns, respectively (Table S2), and no significant changes occurred. It was assumed that the bursting mechanism of RFP on Ce/N-CQDs was the fluorescence internal filtration effect.[34]

2.5. Optimization of Experimental Conditions. The effects of pH, buffer type, and buffer dosage on the detection performance of the sensor were investigated. The results showed that the fluorescence variation tended to be stable in the pH range of 6.0−12.0 (Figure 5a). Therefore, pH 7.4 was chosen for subsequent experiments because it is close to the human pH environment. The effect of different buffer solutions on the system at pH = 7.4 was demonstrated (Figure S5). It can be seen that the best detection performance of the sensor was achieved when 1.00 mL of tris-HCl buffer solution with pH 7.4 was added (Figure 5b).

In order to obtain the sensor's most sensitive detection of RFP, the effects of experimental variables including the amount of Ce/N-CQDs, reaction time, and temperature were investigated. 1.00 mL of tris-HCl buffer solution with pH = 7.4 and 1.00 mL of RFP with a concentration of 1.0×10^{-4} mol/L were taken, and different amounts of Ce/N-CQDs diluted 500 times were added to a 10 mL colorimetric tube. The system fluorescence quenching effect was best when 1.8 mL of Ce/N-CQDs was added to the system (Figure 6a). At room temperature, the fluorescence intensity of the system remained constant for at least 3 h (Figure 6b). With the increase of the reaction temperature, the quenching effect of the system gradually decreased and the best quenching effect was achieved at room temperature (Figure 6c). The system was chosen to be measured after 5 min of reaction at room temperature.

The interaction of common antituberculosis drugs rifampicin (RFP), isoniazid (INH), pyrazinamide (PZA), and ethambutol (EMB) on Ce/N-CQDs was investigated under experimental conditions. It was found that RFP had a significant fluorescence quenching effect on Ce/N-CQDs (Figure 7a). The results show that Ce/N-CQDs have good

https://doi.org/10.1021/acsomega.3c04242
ACS Omega 2023, 8, 34859−34867

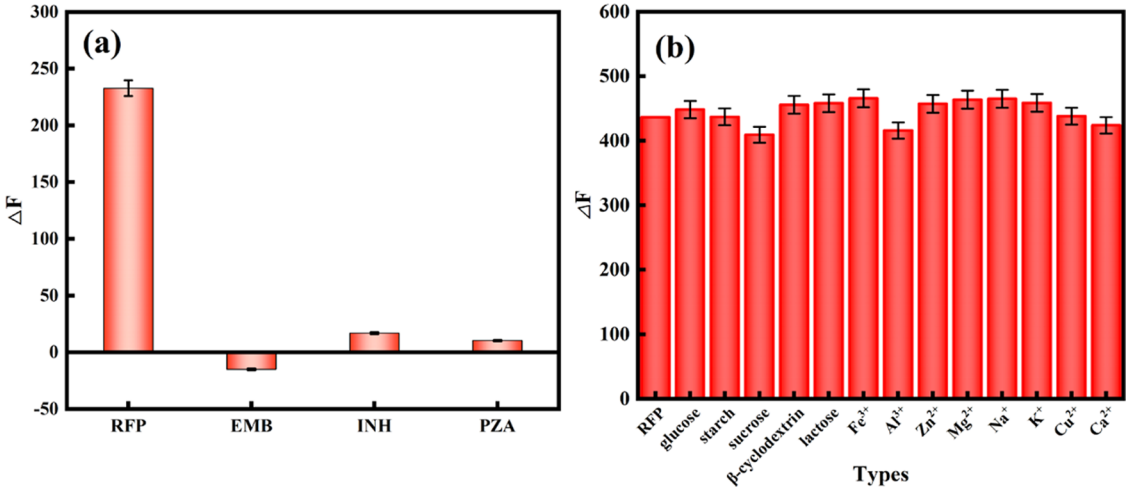

Figure 7. (a) Fluorescence intensity difference (ΔF) of the Ce/N-CQD solution in the absence and presence of 10 μM of various individual antituberculosis drugs. (b) Influence of possible coexisting excipients and some ions on fluorescence intensity.

selectivity for RFP. In addition, the effects of excipients, which may exist in RFP and some other ions on the detection of 1.0 × 10^{-6} mol/L RFP, were examined (Figure 7b). The results demonstrate that 500-fold of glucose, sucrose, lactose, Zn^{2+}, 1000-fold of starch and β-cyclodextrin, 2-fold of Fe^{3+}, 200-fold of Al^{3+}, 50-fold of Mg^{2+}, and 100-fold of Na^{+}, K^{+}, Cu^{2+}, and Ca^{2+} do not alter the signal of the system. It indicated that the prepared Ce/N-CQDs had good selectivity and anti-interference for the determination of RFP.

2.6. Standard Curve. The sensing effect of Ce/N-CQDs as fluorescent probes was investigated under optimal conditions. As shown in Figure 8, the fluorescence intensity

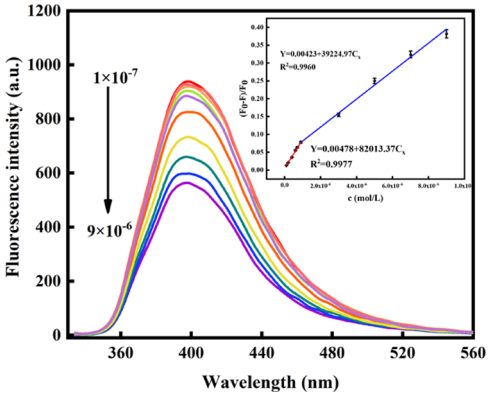

Figure 8. Calibration curve and corresponding fluorescence spectra for RFP.

at 395 nm decreases gradually with the addition of RFP; a good linearity between the quenching efficiency of $(F_0 - F)/F_0$ and the concentrations of RFP was in the range of 1.0 × 10^{-7}–9.0 × 10^{-6} mol/L for RFP. The regression equations were $(F_0 - F)/F_0$ = 0.0042 + 39224.97c (R^2 = 0.9960) and $(F_0 - F)/F_0$ = 0.0048 + 82013.37c (R^2 = 0.9977). According to the formula ($c = 3\sigma/k$), the limit of detection is 9.6 × 10^{-8} mol/L.

The obtained linear range and detection limit were compared with data from other RFP sensors (Table 1). The results showed that the detection method in this experiment has a wider linear range and a lower detection limit.

2.7. Real-Sample Analysis. To evaluate the precision and accuracy of the developed fluorescence probe, the detection of

Table 1. Comparison of the Methods for the Determination of RFP

detection method	detection range (μM)	detection limit (μM)	literature
micellar liquid chromatography	0.060–5.66	0.04	35
fluorescence method (shell core structure composite)	10.00–200.00	8.50	36
electrochemical method	0.080–15.00	0.03	37
fluorescence method (carbon quantum dots embedded in water condensation ball)	2.40–33.80	0.46	38
voltammetry	0.49–303.79	0.15	39
quantum dots (CdTe/ZnS QDs)	4.05–36.45	0.06	40
carbon quantum dots (CQDs)	0.10–9.00	0.09	this work

RFP was performed in RFP capsules as well as human blood serum. Ten RFP capsules were randomly selected from the same batch for spiked recovery experiments. As summarized (Table 2), the recovery of RFP ranged from 95.20% to 101.3%. Compared with other literatures, the method developed in this study was rapid, environmentally friendly, has a wide linear range, and inexpensive.

RFP in human serum samples was analyzed by a standard addition method. The human serum was pretreated with blood collected from healthy people. The recovery data is shown in Table 3. These recoveries were 96.16–102.2% with relative standard deviations less than 5%. It was indicated that the constructed method can be applied to detect RFP in serum samples.

3. CONCLUSIONS

Ce/N-CQDs were synthesized by the codoping of Ce and N using discarded cinnamon nuclei as the carbon source. The codoping of Ce and N not only changed the structure of single CQDs, enriched their surface functional groups, and improved their fluorescence properties but also significantly improved the quantum yields of CQDs. In addition, Ce/N-CQDs exhibit excitation-independent PL characteristics in the excitation wavelength range of 270–350 nm. This study demonstrates the great potential of metal and nonmetal codoping processes in controlling the properties of CQDs. The method is sensitive

https://doi.org/10.1021/acsomega.3c04242
ACS Omega 2023, 8, 34859–34867

Table 2. Capsule Sample Content Determination and Spiked Recovery Test (n = 5)

sample	labeled quantity (mg)	measured (mg)	add (10^{-7} mol/L)	add the measured value (10^{-7} mol/L)	recovery (%)	RSD (%)
1	150.0	150.1	10.00	10.01	100.1	2.3
	150.0	147.3	30.00	29.50	98.33	2.8
	150.0	151.9	50.00	50.64	101.3	1.4
2	150.0	142.9	10.00	9.520	95.20	2.7
	150.0	149.9	30.00	30.01	1.000	3.3
	150.0	144.6	50.00	48.21	96.42	2.5
3	150.0	146.3	10.00	9.750	97.50	1.5
	150.0	148.1	30.00	29.66	98.86	1.3
	150.0	151.6	50.00	50.56	101.1	2.4

Sample source: 1, Shanghai Xinyi Vientiane; 2, Shenyang Hongqi; and 3, Chengdu Jinhua.

Table 3. Determination of Human Serum Sample Content and Spiked Recovery Rate Test (*n* = 5)

sample	original found (10^{-6} mol/L)	add (10^{-6} mol/L)	add the measured value (10^{-6} mol/L)	recovery (%)	RSD (%)
1	0	2.00	2.044	102.2	2.4
2	0	3.00	2.923	97.43	3.4
3	0	5.00	4.808	96.16	1.4

and feasible for the detection of RFP capsules and determination of RFP in human serum. It also has the potential to be used for biomedical analysis.

■ ASSOCIATED CONTENT

Supporting Information

The Supporting Information is available free of charge at https://pubs.acs.org/doi/10.1021/acsomega.3c04242.

Optimization of synthesis conditions for CQDs and Ce/N-CQDs; TEM and particle size distribution of CQDs; XRD spectra of CQDs and Ce/N-CQDs; FTIR spectra of CQDs and Ce/N-CQDs; excitation independence spectra of Ce/N-CQDs; fluorescence quantum yield of CQDs before and after doping; fluorescence lifetime of Ce/N-CQDs; and the impact of buffer types on the sensing system (PDF)

■ AUTHOR INFORMATION

Corresponding Author

Xue-Hua Sun − *Shaanxi Key Laboratory of Chemical Reaction Engineering, College of Chemistry and Chemical Engineering, Yan'an University, Yan'an 716000, P. R. China;* orcid.org/0009-0005-3648-8778; Phone: +86-0911-2332317; Email: happyxh908080@163.com

Authors

Min Ma − *Shaanxi Key Laboratory of Chemical Reaction Engineering, College of Chemistry and Chemical Engineering, Yan'an University, Yan'an 716000, P. R. China*

Rui Tian − *Shaanxi Key Laboratory of Chemical Reaction Engineering, College of Chemistry and Chemical Engineering, Yan'an University, Yan'an 716000, P. R. China*

Hong-Mei Chai − *Shaanxi Key Laboratory of Chemical Reaction Engineering, College of Chemistry and Chemical Engineering, Yan'an University, Yan'an 716000, P. R. China;* orcid.org/0000-0001-8555-4421

Jian-Wei Wang − *Shaanxi Key Laboratory of Chemical Reaction Engineering, College of Chemistry and Chemical Engineering, Yan'an University, Yan'an 716000, P. R. China;* orcid.org/0000-0003-3754-0150

Lou-Jun Gao − *Shaanxi Key Laboratory of Chemical Reaction Engineering, College of Chemistry and Chemical Engineering, Yan'an University, Yan'an 716000, P. R. China;* orcid.org/0000-0003-3616-4325

Complete contact information is available at: https://pubs.acs.org/10.1021/acsomega.3c04242

Notes

The authors declare no competing financial interest.

■ ACKNOWLEDGMENTS

This work was supported by the National Natural Science Foundation of China (No. 22063010) and the Scientific Research Program of the Shaanxi Provincial Department of Science and Technology (No. 2022QFY07-05).

■ REFERENCES

(1) Smith, T. C.; Aldridge, B. B. Targeting drugs for tuberculosis. *Science* **2019**, *364*, 1234−1235.

(2) Grobbelaar, M.; Louw, G. E.; Sampson, S. L.; Helden, P. D.; Donald, P. R.; Warren, R. M. Evolution of rifampicin treatment for tuberculosis. *Infect., Genet. Evol.* **2019**, *74*, 103937−103961.

(3) Park, S.; Jo, K. W.; Lee, S. D.; Kim, W. S.; Shim, T. S. Treatment outcomes of rifampin-sparing treatment in patients with pulmonary tuberculosis with rifampin-mono-resistance or rifampin adverse events: A retrospective cohort analysis. *Respir. Med.* **2017**, *131*, 43−48.

(4) Amidi, S.; Ardakani, Y. H.; Amiri-Aref, M.; Ranjbari, E.; Sepehri, Z.; Bagheri, H. Sensitive electrochemical determination of rifampicin using gold nanoparticles/poly-mela- mine nanocomposite. *RSC Adv.* **2017**, *7*, 40111−40118.

(5) Bravo, M. Á. G.; Durgbanshi, A.; Bose, D.; Mishra, P.; Albiol-Chiva, J.; Esteve-Romero, J.; Peris-Vicente, J. Quantification of rifampicin and rifabutin in plasma of tuberculosis patients by micellar liquid chromatography. *Microchem J.* **2020**, *157*, 104865−104873.

(6) Shokri, R.; Amjadi, M. Boron and nitrogen co-doped carbon dots as a chemiluminescence probe for sensitive assay of rifampicin. *J. Photochem. Photobiol. A Chem.* **2022**, *425*, No. 113694.

(7) Li, X. C.; Zhao, S. J.; Li, B. L.; Yang, K.; Lan, M. H.; Zeng, L. T. Advances and perspectives in carbon dot-based fluorescent probes: Mechanism, and application. *Coordin. Chem. Rev.* **2021**, *431*, 213686−213707.

(8) Tayyebi, A.; Akhavan, O.; Lee, B. K.; Outokesh, M. Supercritical water in top-down formation of tunable-sized graphene quantum dots applicable in effective photothermal treatments of tissues. *Carbon* **2018**, *130*, 267−272.

(9) Rabiee, N.; Sharma, R.; Foorginezhad, S.; Jouyandeh, M.; Asadnia, M.; Rabiee, M.; Akhavan, O.; Lima, E. C.; Formela, K.; Ashrafizadeh, M.; Fallah, Z.; Hassanpour, M.; Mohammadi, A.; Saeb, M. R. Green and Sustainable Membranes: A review. *Environ. Res.* **2023**, *231*, 116133−116175.
(10) Rajendran, S.; Ushavipinachandran, V.; Haroon, K. H. B.; Ashokan, I.; Bhunia, S. K. A comprehensive review on multi-colored emissive carbon dots as fluorescent probes for the detection of pharmaceutical drugs in water. *Anal. Methods* **2022**, *14*, 4263−4291.
(11) Torres Landa, S. D.; Bogireddy, N. K. R.; Kaur, I.; Batra, V.; Agarwal, V. Heavy metal ion detection using green precursor derived carbon dots. *iScience* **2022**, *25*, 103816−103850.
(12) Yuan, X. T.; Tu, Y. J.; Chen, W.; Xu, Z. W.; Wei, Y. L.; Qin, K. H.; Zhang, Q.; Xiang, Y. Y.; Zhang, H. G.; Ji, X. L. Facile synthesis of carbon dots derived from ampicillin sodium for live/dead microbe differentiation, bioimaging and high selectivity detection of 2,4-dinitrophenol and Hg (II). *Dyes Pigments* **2020**, *175*, 108187−108196.
(13) Zhao, F. N.; Wu, J.; Ying, Y. B.; She, Y. X.; Wang, J.; Ping, J. F. Carbon nanomaterial-enabled pesticide biosensors: Design strategy, biosensing mechanism, and practical application. *TrAC, Trends Anal. Chem.* **2018**, *106*, 62−83.
(14) Shahcheraghi, N.; Golchin, H.; Sadri, Z.; Tabari, Y.; Borhanifar, F.; Makani, S. Nano-biotechnology, an applicable approach for sustainable future. *3 Biotech* **2022**, *12*, 65−89.
(15) Wareing, T. C.; Gentile, P.; Phan, A. N. Biomass-Based Carbon Dots: Current Development and Future Perspectives. *ACS Nano* **2021**, *15*, 15471−15501.
(16) Wu, S. H.; Zhou, R. H.; Chen, H. J.; Zhang, J. Y.; Wu, P. Highly efficient oxygen photosensitization of carbon dots: the role of nitrogen doping. *Nanoscale* **2020**, *12*, 5543−5553.
(17) Guo, Y. Z.; Liu, J. L.; Chen, Y. F.; Chai, Y. Q.; Li, Z. H.; Yuan, R. Boron and Nitrogen-Co doped Carbon Dots as Highly Efficient Electrochemiluminescence Emitters for Ultrasensitive Detection of Hepatitis B Virus DNA. *Anal. Chem.* **2022**, *94*, 7601−7608.
(18) Lu, H. Z.; Li, C. C.; Wang, H. H.; Wang, X. M.; Xu, S. F. Biomass-Derived Sulfur, Nitrogen Co-Doped Carbon Dots for Colorimetric and Fluorescent Dual Mode Detection of Silver (I) and Cell Imaging. *ACS Omega* **2019**, *4*, 21500−21508.
(19) Wang, W. X.; Chen, J.; Wang, D.; Shen, Y.; Yang, L.; Zhang, T.; Ge, J. Facile synthesis of biomass waste-derived fluorescent N, S, P co-doped carbon dots for detection of Fe^{3+} ions in solutions and living cells. *Anal. Methods* **2021**, *13*, 789−795.
(20) Niu, N.; Fu, L. X.; Liu, T.; Yang, F.; Wu, M.; Yin, C. H.; Chen, L. G. A multi-channel array for metal ions discrimination with animal bones derived biomass carbon dots as sensing units. *J. Photochem. Photobiol., A* **2022**, *424*, 113638−113648.
(21) Liu, H. C.; Ding, J.; Zhang, K.; Ding, L. Construction of Biomass Carbon Dots Based Fluorescence Sensors and Their Applications in Chemical and Biological Analysis. *TrAC Trends Anal. Chem.* **2019**, *118*, 315−337.
(22) Yuxin, X.; Sun, L. P.; Liu, K.; Shi, H. P.; Wang, Z. H.; Wang, W. J. Metal-doped carbon dots as peroxidase mimic for hydrogen peroxide and glucose detection. *Anal. Bioanal. Chem.* **2022**, *414*, 5857−5867.
(23) Han, C. Y.; Zhang, X. M.; Wang, F.; Yu, Q. H.; Chen, F.; Shen, D.; Yang, Z. Y.; Wang, T. T.; Jiang, M. Y.; Deng, T.; Yu, C. Duplex metal co-doped carbon quantum dots-based drug delivery system with intelligent adjustable size as adjuvant for synergistic cancer therapy. *Carbon* **2021**, *183*, 789−808.
(24) Wang, Y. J.; Chen, J.; Liu, L. M.; Xi, X. X.; Li, Y. M.; Geng, Z. L.; Jiang, G. Y.; Zhao, Z. Novel metal doped carbon quantum dots/CdS composites for efficient photocatalytic hydrogen evolution. *Nanoscale.* **2019**, *11*, 1618−1625.
(25) CHEN, F.; Lihua, Z.; Hong, W. Preparation of Carbon Dots and Determination of Their Fluorescence Quantum Yield. *Univ. Chem.* **2019**, *34*, 67−72.
(26) Yao, S. Z.; Wu, Q. Q.; Fang, A. J.; Li, H. T.; Zhang, Y. Y. Enzymatic-induced upconversion photoinduced electron transfer for sensing tyrosine in human serum. *Biosens. Bioelectron.* **2016**, *77*, 957−962.
(27) Du, F. Y.; Zhang, M. M.; Ju, H. X.; Zhang, L.; Sun, M. Z.; Zhou, Z. W.; Dai, Z. Y.; Zhang, L. R.; Gong, A. H.; Wu, C. Y. Engineering iodine-doped carbon dots as dual-modal probes for fluorescence and X-ray CT imaging. *Int. J. Nanomed.* **2015**, *10*, 6943−6953.
(28) Shen, T.; Wang, Q.; Guo, Z. Hydrothermal synthesis of carbon quantum dots using different precursors and their combination with TiO_2 for enhanced photocatalytic activity. *Ceram. Int.* **2018**, *44*, 11828−11834.
(29) Larachi, F.; Pierre, J.; Adnot, A.; Bernis, A. Ce 3d XPS study of composite $Ce_xMn_{1-x}O_{2-y}$ wet oxidation catalysts. *Appl. Surf. Sci.* **2002**, *195*, 236−250.
(30) Zhang, M. Z.; Zhai, X. Y.; Ma, T. F.; Huang, Y. K.; Yan, C. H.; Du, Y. P. Multifunctional cerium doped carbon dots nanoplatform and its applications for wound healing. *Chem. Eng. J.* **2021**, *423*, 130301−130326.
(31) Zhang, Y. Q.; Hu, Y. S.; Lin, J.; Fan, Y.; Li, Y. T.; Lv, Y.; Liu, X. Y. Excitation Wavelength Independence: Toward Low-Threshold Amplified Spontaneous Emission from Carbon Nanodots. *ACS Appl. Mater. Interfaces* **2016**, *8*, 25454−25460.
(32) Gong, Y.; Dong, Z. H. Transfer, transportation, and accumulation of cerium-doped carbon quantum dots: Promoting growth and development in wheat. *Ecotoxicol. Environ. Saf.* **2021**, *226*, 112852−112861.
(33) Zhu, C.; Yang, S. W.; Wang, G.; Mo, R. W.; He, P.; Sun, J.; Di, Z. F.; Yuan, N. Y.; Ding, J. N.; Ding, G. Q.; Xie, X. M. Negative induction effect of graphite N on graphene quantum dots: tunable band gap photoluminescence. *J. Mater. Chem. C* **2015**, *3*, 8810−8816.
(34) Yang, L.; Wen, J. X.; Li, K. J.; Liu, L.; Wang, W. Carbon quantum dots: Comprehensively understanding of the internal quenching mechanism and application for catechol detection. *Sens. Actuators, B* **2021**, *333*, 129557−129566.
(35) Bravo, M. Á. G.; Durgbanshi, A.; Bose, D.; Mishra, P.; Albiol-Chiva, J.; Esteve-Romero, J.; Peris-Vicente, J. Quantification of rifampicin and rifabutin in plasma of tuberculosis patients by micellar liquid chromatography. *Microchem. J.* **2020**, *157*, 104865−104873.
(36) Su, J.; Xiang, X. F.; Lv, R.; Li, H.; Fu, X.; Yang, B. Y.; Gu, W.; Liu, X. Rapid and high-selectivity detection of rifampicin based on upconversion luminescence core-shell structure composites. *J. Solid State Chem.* **2018**, *266*, 9−15.
(37) Amidi, S.; Ardakani, Y. H.; Amiri-Aref, M.; Ranjbari, E.; Sepehri, Z.; Bagheri, H. Sensitive electrochemical determination of rifampicin using gold nanoparticles/poly-me- lamine nanocomposite. *RSC Adv.* **2017**, *7*, 40111−40118.
(38) Li, Y. H.; Mou, C. J.; Xie, Z. G.; Zheng, M. Carbon dots embedded hydrogel spheres for sensing and removing rifampicin. *Dyes Pigments* **2022**, *198*, 110023−110028.
(39) Szlósarczyk, M.; Piech, R.; Milc, A.; Hubicka, U. Fast and Sensitive Voltammetric Method for the Determination of Rifampicin on Renewable Amalgam Film Electrode. *Sensors* **2021**, *21*, 5792−5800.
(40) Hooshyar, Z.; Bardajee, G. R. Fluorescence enhancement of glutathione capped CdTe/ZnS quantum dots by embedding into cationic starch for sensitive detection of rifampicin. *Spectrochim. Acta, Part A* **2017**, *173*, 144−150.

https://doi.org/10.1021/acsomega.3c04242
ACS Omega 2023, 8, 34859−34867